Role of Asian summer monsoon subsystems in the inter-hemispheric progression of deglaciation

K. Nilsson-Kerr[1*], P. Anand[1], P. F. Sexton[1], M. J. Leng[2], S. Misra[3], S. C. Clemens[4], S. J. Hammond[1]

[1]School of Environment, Earth and Ecosystem Sciences, Faculty of Science, Technology, Engineering and Mathematics, The Open University, Milton Keynes, MK76AA, UK

[2]NERC Isotope Geoscience Facilities, British Geological Survey, Nottingham, NH125GG, UK and Centre for Environmental Geochemistry, School of Biosciences, Sutton Bonington Campus, University of Nottingham, Loughborough, LE12 5RD, UK

[3]Centre for Earth Sciences, Indian Institute of Science, Bangalore, 560012, India

[4]Earth, Environmental, and Planetary Sciences, Brown University, Providence, 02912, USA

([*]katrina.kerr@open.ac.uk)

The response of Asian Monsoon subsystems to both hemispheric climate forcing and external orbital forcing are currently issues of vigorous debate. The Indian Summer Monsoon is the dominant monsoon subsystem in terms of energy flux, constituting one of Earth's most dynamic expressions of ocean-atmosphere interactions. Yet the Indian Summer Monsoon is grossly under-represented in Asian Monsoon palaeoclimate records. Here we present high-resolution records of Indian Summer Monsoon induced rainfall and fluvial runoff recovered in a sediment core from the Bay of Bengal across Termination II, 139 to 127 thousand years ago, including coupled measurements of the oxygen isotopic composition and Mg/Ca, Mn/Ca, Nd/Ca and U/Ca ratios in surface-ocean dwelling foraminifera. Our data reveal a millennial-scale transient strengthening of the Asian Monsoon that punctuates Termination II associated with an oscillation of the

bipolar seesaw. The progression of deglacial warming across Termination II emerges first in the southern hemisphere then the tropics in tandem with Indian Summer Monsoon strengthening and finally the northern hemisphere. We therefore suggest that the Indian Summer Monsoon was a conduit for conveying southern hemisphere latent heat northwards, thereby promoting subsequent northern hemisphere deglaciation.

Early modelling studies that attempted to evaluate the response of the boreal summer monsoon to orbital forcing identified Northern Hemisphere (NH) solar insolation (during precession$_{min}$) as a primary driver, via its influence on land-ocean thermal contrasts[1]. Palaeoclimate records of the ISM support this view but also commonly invoke NH climate controls[2] owing to the coincidence of weak Indian Summer Monsoon (ISM) intervals with North Atlantic Heinrich Events[2, 3]. These millennial scale cooling events originating in the high latitudes of the NH have been linked to the ISM via atmospheric[3] and oceanic[4] teleconnections. Similarly, East Asian Summer Monsoon (EASM) speleothem oxygen isotope ($\delta^{18}O$) records, inferred to reflect both upstream depletion of $\delta^{18}O$ from tropical moisture sources and regional precipitation amount[5], have been linked to both NH solar insolation and North Atlantic forcing[6], although this interpretation has been recently questioned in light of new EASM rainfall records[7, 8]. Despite this prevailing view of NH forcing of the Asian Monsoon on millennial to orbital timescales, some observations from ISM records have pointed to additional mechanisms influencing ISM behaviour[9-11]. The nature of variance in the obliquity band and lag of ISM maxima with precession$_{min}$ suggests a component of Southern Hemisphere (SH) forcing through latent heat export[9, 10]. Understanding of the ISM at timescales beyond the last glacial period mainly derives from orbital-scale records from the Arabian Sea and southern Bay of Bengal (BoB) (Fig. 1a). Records from these locations have applied proxies that have been assumed to be representative of upwelling and changes in water column stratification driven by ISM winds. However, the extent to which the ISM exclusively controls these proxies

remains unclear. Thus, what is urgently required to enhance our understanding of the ISM are records of rainfall and runoff from the ISM's core convective region, the northern BoB in order to isolate a primary and direct signal of ISM strength.

Here we report new geochemical records from well preserved planktic foraminifera at a sub-millennial scale resolution (~250-500 years) spanning Termination II (TII, 139 to 127 thousand years ago (ka)) from IODP 353, Site U1446 in the northern BoB. Site U1446 is situated in the core convective region of the ISM, under the direct influence of ISM-induced rainfall and fluvial runoff received from one of the world's largest river systems (Ganges-Brahmaputra). Figure 1(b-e) shows the southward propagation of the ISM induced freshwater plume derived from the Ganges-Brahmaputra systems, engulfing Site U1446 during the peak summer monsoon season. This site is thus ideally situated to capture the signal of ISM derived rainfall, fluvial runoff and sediment delivery from the Indian subcontinent. We have produced a detailed stratigraphy for Site U1446 that is tied to the Antarctic Ice Core (AICC2012) chronology[12] (Methods, Supplementary Fig. 1). To evaluate changes in the surface ocean salinity response to rainfall and runoff, we combine oxygen isotope ($\delta^{18}O_c$) and Mg/Ca-derived SSTs from the planktic foraminifera *Globigerinoides ruber (sensu-stricto)* to reconstruct $\delta^{18}O$ of seawater ($\delta^{18}O_{sw}$) (Methods) (Fig. 2B n).

We also present Mn/Ca, Nd/Ca and U/Ca ratios (Supplementary Fig. 8) of *G. ruber ss* calcite in a novel application to reconstruct fluvial runoff, where high concentrations of Mn, Nd and U are delivered from the continental hinterland by the ISM's vigorous hydrological and weathering regime[13-15]. This regime exerts a strong seasonal bias on the vertical and lateral distribution of dissolved 'lithogenic' elements within the BoB[14], with a strong lithogenic signal existing in the upper 100m of the northern BoB as a result of high terrigenous fluxes[15]. The origin of Nd in planktic foraminiferal calcite remains controversial with the Nd being attributed to either reflect in-situ seawater Nd signal[16], a mixed signal from sediments and bottom

waters[17] or to arise from intra-test organic matter[18]. We interpret our foraminiferal Mn/Ca, Nd/Ca and U/Ca data to reflect a primary signal of upper ocean chemistry modulated by high fluxes of lithogenic elements from high fluvial runoff for several reasons. First, the foraminifera cleaning method we applied included a reductive cleaning step that ensures removal of Fe-Mn coatings added on the foraminifera test at the sediment-water interface[19]. Second, Mn/Ca correlates with Nd/Ca and U/Ca (Supplementary Fig. 7), suggesting that the concentrations of these elements are all derived from the same dominant process (i.e. in this hydrographic setting, fluvial runoff). Third, the concentrations of lithogenic elements in modern seawater in the northern BoB are much higher than for global average seawater[15] (owing to high dissolved elemental fluxes from the continent, driven by the ISM). Fourth, the observed concentrations of these elements are beyond what is typically found in planktic foraminifera[20]. We normalised Mn/Ca, Nd/Ca and U/Ca to unit variance[21] to produce a stack of *G. ruber ss* geochemical tracers of fluvial runoff (Fig. 2B m) (Methods). The range of values exhibited by this runoff tracers record overlaps with the range of these same elements in modern *G. ruber ss* as measured from a 2005 sediment trap in the northern BoB (red vertical bar in Fig. 2B m). This underscores that our *G. ruber ss*-based stacked record of Mn, Nd and U concentrations is recording high concentrations of these elements in local seawater (derived from high runoff fluxes), rather than being a post-depositional phenomenon via diagenetic alteration of the foraminiferal calcite. Therefore, comparing *G. ruber ss* $\delta^{18}O_{sw}$ and *G. ruber ss* runoff tracers together provides a novel opportunity to reconstruct changes in both salinity and fluvial runoff sourced directly from the ISM. Application of these runoff tracers in *G. ruber ss* as representing ISM river fluxes is supported by elemental signatures of continental origin from discrete portable X-Ray Fluorescence (pXRF) measurements on bulk sediment samples that are purely diagnostic of continental detrital input from runoff (Al, Ti, K, Rb) (Fig. 2B l) (Methods, Supplementary Fig. 9).

Our high-resolution time series of $\delta^{18}O_{sw}$, *G. ruber ss* runoff tracers and pXRF element stack show a similar pattern of ISM behaviour across TII, accounting for the differing intensity in the response and thresholds between surface freshening and riverine sediment fluxes[22]. The data reveal a brief intensification of the ISM from ~134 to 133 ka, reflected as a decrease in $\delta^{18}O_{sw}$ (Fig. 2B n), an increase in *G. ruber ss* runoff tracers (Fig. 2B m), and pXRF element stack (Fig. 2B l) late in Marine Isotope Stage (MIS) 6, prior to TII onset. This was immediately preceded by a ~1 kyr duration SST warming in the BoB (Fig. 2B o), suggesting advection of SH heat across the equator provided a crucial precondition[23] for the subsequent transient strengthening of monsoonal circulation at 134 ka. Our data show that the ISM then undergoes two phases of deglacial strengthening; first at ~131 to 130 ka, followed by a further strengthening at ~129 ka, with the final attainment of a vigorous interglacial ISM coeval with the development of full deglaciation into the Last Interglacial (MIS 5e) (Fig. 2B).

Interstadial within Termination II

The structure of the last two terminations, TI and TII, is fundamentally different (Fig. 2, Methods). TI is punctuated by several millennial scale events, manifested in the Bølling-Allerød and Younger Dryas, associated with fluctuations in Atlantic Meridional Overturning Circulation (AMOC)[24] (Fig. 2A). Such millennial scale events have remained largely unidentified in reconstructions of TII. However, we identify a climatic event punctuating TII, evident in ISM rainfall and runoff (Fig. 2B l, m and n) at ~134 to 133 ka, prior to the timing of TII deglaciation in the NH[25]. We refer to this event as the Termination II Interstadial (TII IS). ISM strengthening during the TII IS was preceded by a 1ºC warming in *G. ruber ss* derived SSTs at ~135 ka (Fig. 2B o). This warming coincides with early deglaciation in the SH (Fig. 2B i, k) but with the establishment of cool condition in the North Atlantic associated with Heinrich Stadial 11 (HS11) onset[26]. We infer that this SST warming in the BoB reflects cross-equatorial heat transport in response to contemporaneous warming in the SH. These SH-

derived energy fluxes, advecting northwards, leads to the transient strengthening of the ISM that marks the TII IS (Fig. 2B l, m and n). We thus attribute the TII IS to a transient oscillation of the bipolar seesaw, akin to mechanisms proposed for TI[24, 27]. The TII IS is also depicted in other NH records, a western Mediterranean Sea SST record[26, 28] (Fig. 2B f) and the EASM speleothem $\delta^{18}O$ record[6, 29] (Fig. 2B e). Further support for a cross-equatorial northward flux of SH-derived heat through a bipolar seesaw mechanism is provided by a cooling in the South-East Atlantic coeval with the TII IS, which has been attributed to a reduction in Agulhas Leakage associated with a northward shift of the atmospheric belts towards the warmer (northern) hemisphere[30]. The timing of TII IS is within error of Meltwater Pulse 2B (MWP 2B, 133±1 ka)[26]. Thus, it appears that TII IS may have contributed to rapid retreat of NH ice sheets and the resulting MWP 2B owing to heat import into the NH. The resulting enhanced freshwater fluxes into the North Atlantic[31] causes an intensification of HS11 (Fig. 2B c, d), cooling of the NH and the ending of TII IS associated with a southward shift of the Inter-Tropical Convergence Zone (ITCZ)[32]. Recent work has argued for a robust North Atlantic control on the EASM[6, 29]. Yet our findings for a SH origin for the transient EASM strengthening during TII IS, perhaps via the ISM, reveal that the nature of these inter-hemispheric controls on a given monsoonal subsystem is not fixed, but dynamic across different timescales.

Inter-hemispheric progression of deglaciation

The nature of deglaciation during TII is thought to be a result of orbital preconditioning; an earlier maximum in SH solar insolation 10 kyr prior to NH solar insolation maxima promoting earlier Antarctic warming[25] (Fig 2B b). Furthermore, obliquity_{max} (Fig. 2B a) was reached prior to precession_{min}[33] (Fig. 2B b), triggering an increased inter-hemispheric temperature contrast and strengthening of the Hadley Cell in the warmer (southern) hemisphere. The colder (northern) hemisphere is compensated by increased cross-equatorial heat transport[34]. Figure 3 shows the statistically determined timings[35] of regional deglaciation throughout TII. The

combination of obliquity$_{max}$ and early deglacial SH warming (Fig. 3h) dictates that heat and moisture transported to the ISM would have been across the equator from the southern Indian Ocean. We thus conclude that SH sourced energy fluxes (Fig. 3h) were responsible for early deglacial strengthening of the ISM at ~131 to 130 ka (Fig. 3e-g). A contemporaneous early deglacial warming occurs in the western Mediterranean[26, 28] (Fig. 3d) that we infer reflects adiabatic descent from the descending limb of the Hadley Cell[36], propagating SH sourced energy fluxes northward. This northward propagation of SH heat and moisture into higher NH latitudes was slowed by the persistence of a cold North Atlantic with HS11 (Fig. 3a, b). Subsequently, the inter-hemispheric progression of deglacial warming is propagated into the higher latitudes of the North Atlantic (Fig. 3a, b) with associated EASM strengthening (Fig. 3c). Our ISM records (Fig. 2B m, n) show strong covariance with the Antarctic CH_4 record (Fig. 2B j) during both the TII IS and broader deglaciation. This finding supports hypotheses that call for tropical wetlands as being an important global methane source during glacial-interglacial transitions and that the tropical monsoonal system plays a fundamental role in regulating concentrations of this greenhouse gas[37].

Millennial-scale phasing of Asian Monsoon subsystems

Our ISM records across TII provide insights into the relationship between the two main Asian Monsoon subsystems at the millennial scale. Deglacial ISM strengthening is temporally decoupled from EASM strengthening by ~1 to 2 kyr (Fig. 3). We infer that this lag is not associated with respective age-models and instead ultimately reflects the time transgressive nature of deglacial strengthening in the Asian Monsoon subsystems and influence of differing forcing mechanisms triggering this strengthening. The makeup of these two monsoonal subsystems is quite different; differing land-ocean configurations, atmospheric and ocean dynamics[38] thus, it is likely that during major changes in background climate state the ISM and EASM exhibit such time-transgressive responses.

Our findings thus allow us to reject the hypothesis of a singular common (NH) forcing mechanism of the Asian Monsoon[6]. Therefore, despite the iconic nature of the EASM speleothem records[6], our high-resolution ISM rainfall and runoff data suggest that the assumption that they are representative of the Asian Monsoon as a whole needs to be reconsidered, at least on millennial timescales. This decoupling of the ISM and EASM across TII may owe its origins to the complexities and large-scale variation in the moisture supply amalgamated in the speleothem $\delta^{18}O$ signal[8, 39]. Our new records point to a greater dynamism in the mechanisms regulating Asian Monsoon rainfall beyond just teleconnections to the North Atlantic[6]. This emphasises the need for more high-resolution palaeoclimate time series that are directly influenced by monsoonal rainfall, for both the EASM and ISM, in order to shed further light on the mechanism and feedbacks regulating monsoonal subsystems.

Our findings from TII indicate that the ISM is a key inter-hemispheric link in the transfer of heat and moisture between the warm SH into the colder NH (Fig. 3). Our sub-millennial scale records provide support for hypotheses that argue for an important role of the tropics[40] in conveying SH latent heat northwards into the NH, thereby promoting NH deglaciation. However, the evolution of the ISM captured in our data suggests that a fully strengthened 'interglacial' mode of the ISM cannot be attained until the NH experiences full deglacial climatic amelioration (Fig. 3). Our results highlight the need for explicit differentiation between the ISM and EASM owing to their respective sensitivities to fundamentally different components of the Earth system during global climate change. Our data also reveal that inter-hemispheric climatic controls on the two primary monsoonal subsystems are dynamic across different timescales and that, during a glacial transition, these two monsoonal subsystems can be governed by different inter-hemispheric controls.

References

198 1. Kutzbach, J. E. Monsoon climate of the early Holocene: climate experiment with the
199 Earth's orbital parameters for 9000 years ago. *Science.* **214,** 59-61 (1981).
200 2. Kathayat, G. *et al*. Indian monsoon variability on millennial-orbital timescales. *Sci.*
201 *Rep.* **6,** 24374 (2016).
202 3. Deplazes, G. *et al*. Weakening and strengthening of the Indian monsoon during
203 Heinrich events and Dansgaard-Oeschger oscillations. *Paleoceanography*. **29,**
204 2013PA002509 (2014).
205 4. Tierney, J. E., Pausata, F, S, R. & deMenocal, P. Deglacial Indian monsoon failure and
206 North Atlantic stadials linked by Indian Ocean surface cooling. *Nat. Geosci.* **9,** 46-50
207 (2015).
208 5. Orland, I. J. *et al*. Direct measurements of deglacial monsoon strength in a Chinese
209 stalagmite. *Geology.* **43,** 555-558 (2015).
210 6. Cheng, H. *et al.* The Asian monsoon over the past 640,000 years and ice age
211 terminations. *Nature.* **534,** 640-646 (2016).
212 7. Beck, J. W. *et al.* A 550,000-year record of East Asian monsoon rainfall from ^{10}Be in
213 Loess. *Science.* **360,** 877-881 (2018).
214 8. Clemens, S.C. *et al*. Precession-band variance missing from East Asian monsoon
215 runoff. *Nat. Commun.* **9,** 3364 (2018).
216 9. Clemens, S. C. & Prell, W. L. 350,000 year summer-monsoon multi-proxy from the
217 Owen Ridge, Northern Arabian Sea. *Mar. Geol.* **201,** 35-51 (2003).
218 10. Caley, T. *et al.* New Arabian Sea records help decipher orbital timing of Indo-Asian
219 monsoon. *Earth Planet. Sci. Lett*. **308,** 433-444 (2011).
220 11. Zhisheng, A. *et al*. Glacial-Interglacial Indian Summer Monsoon Dynamics. *Science.*
221 **333,** 719-723 (2011).

12. Bazin, L. *et al*. An optimized multi-proxy, multi-site Antarctic ice and gas orbital chronology (AICC2012): 120-800 ka. *Clim. Past.* **9,** 1715-1731 (2013).
13. Sarin, M. M., Krishnaswami, S., Somayajulu, B. L. K. & Moore, W. S. Chemistry of uranium, thorium, and radium isotopes in the Ganga-Brahmaputra river system: Weathering processes and fluxes into the Bay of Bengal. *Geochim. Cosmochim. Acta.* **54,** 1387-1396 (1990).
14. Singh, S. P. *et al*. Spatial distribution of dissolved neodymium and ε_{Nd} in the Bay of Bengal: Role of particulate matter and mixing of water mass. *Geochim. Cosmochim. Acta.* **94,** 38-56 (2012).
15. Yu, Z. *et al*. Seasonal variations in dissolved neodymium isotope composition in the Bay of Bengal. *Earth Planet. Sci. Lett.* **479,** 310-321 (2017).
16. Vance, D. & Burton, K. Neodymium isotopes in planktonic foraminifera: a record of the response of continental weathering and ocean circulation rates to climate change. *Earth Planet. Sci. Lett.* **173,** 365-379 (1999).
17. Pomiès, C., Davies, G. R. & Conan, S. M. –H. Neodymium in modern foraminifera from the Indian Ocean: implications for the use of foraminiferal Nd isotope compositions in paleo-oceanography. *Earth Planet. Sci. Lett.* **203,** 1031-1045 (2002).
18. Martínez-Botí, M. A., Vance. D. & Mortyn, P. G. Nd/Ca ratios in plankton-towed and core top foraminifera: Confirmation of the water column acquisition of Nd. *Geochem. Geophys. Geosyst.* **10,** Q08018 (2009).
19. Boyle, E. A. & Keigwin, L. D. Comparison of Atlantic and Pacific paleochemical records for the last 215,000 years: changes in deep ocean circulation and chemical inventories. *Earth Planet. Sci. Lett.* **76,** 135-150 (1985).

20. Russell, A. N., Emerson, S., Nelson, B. K., Erez, J. & Lea, D. W. Uranium in foraminiferal calcite as recorder of seawater uranium concentrations. *Geochim. Cosmochim. Acta.* **58,** 671-681 (1994).
21. Abdi, H. *Normalizing data: In Salkind, N. (Ed.), Encyclopoedia of Research Design* (Sage, Thousand Oaks, CA, 2010).
22. Dearing, J. A. & Jones, R. T. Coupling temporal and spatial dimensions of global sediment flux through lake and marine sediment records. *Glob Planet Change.* **39,** 147-168 (2003).
23. McCreary, J. P., Kundu, P. K. & Molinari, R. L. A numerical investigation of dynamics, thermodynamics and mixed-layer processes in the Indian Ocean. *Prog. Oceanog.* **31,** 181-244 (1993).
24. Barker, S. *et al*. Interhemispheric Atlantic seesaw response during the last deglaciation. *Nature*. **457,** 1097-1101 (2009).
25. Broecker, W. S. & Henderson, G. M. The sequence of events surrounding Termination II and their implications for the cause of glacial-interglacial CO2 changes. *Paleoceanography*. **13,** 352-364 (1998).
26. Marino, G. *et al*. Bipolar seesaw control on last interglacial sea level. *Nature*. **522,** 197-201 (2015).
27. Knorr, G. & Lohmann, G. Rapid transitions in the Atlantic thermohaline circulation triggered by global warming and meltwater during the last deglaciation. *Geochem. Geophys. Geosyst*. **8,** Q12006 (2007).
28. Martrat, B., Jimenez-Amat, P., Zahn, R. & Grimalt, J. O. Similarities and dissimilarities between the last two deglaciations and interglaciations in the North Atlantic region. *Quat. Sci. Rev.* **99,** 122-134 (2014).
29. Cheng, H. *et al*. Ice Age Terminations. *Science*. **326,** 248-252 (2009).

30. Scussolini, P., Marino, G., Brummer, G. –J. & Peeters, F. J. C. Saline Indian Ocean waters invaded the South Atlantic thermocline during glacial termination II. *Geology.* **43,** 139-142 (2015).
31. Carlson, A. E. & Winsor, K. Northern Hemisphere ice-sheet responses to past climate warming. *Nat. Geosci*. **5,** 607-613 (2012).
32. Broccoli, A. J., Dahl, K. A. & Stouffer, R. J. Response of the ITCZ to Northern Hemisphere cooling. *Geophys. Res. Lett.* **33,** L01702 (2006).
33. Laskar, J. *et al.* A long-term numerical solution for the insolation quantities of the Earth. *Astron. Astrophys.* **428,** 261-285 (2004).
34. Mantis, D. F. *et al*. The Response of Large-Scale Circulation to Obliquity-Induced Changes in Meridional Heating Gradients. *J. Clim*. **27,** 5504-5516 (2014).
35. Mudelsee, M. Ramp function regression: a tool for quantifying climate transitions. *Comput. Geosci.* **26,** 293-307 (2000).
36. Rodwell, M. J. & Hoskins, B. J. Subtropical Anticyclones and Summer Monsoons. *J. Clim.* **14,** 3192-3211 (2001).
37. Loulergue, L. *et al*. Orbital and millennial-scale features of atmospheric CH_4 over the past 800,000 years. *Nature.* **453,** 383-386 (2008).
38. Wang, B., Clemens, S. C. & Liu, P. Contrasting the Indian and East Asian monsoons: implications on geologic timescales. *Mar. Geol.* **201,** 5-21 (2003).
39. Caley, T., Roche, D. M. and Renssen, H. Orbital Asian summer monsoon dynamics revealed using an isotope-enabled global climate model. *Nat. Commun.* **5,** 5371 (2014).
40. Rodgers, K. B. *et al*. A tropical mechanism for Northern Hemisphere deglaciation. *Geochem. Geophys. Geosyst*. **4,** 1046 (2003).

41. Bolton, C. T. et *al*. A 500,000 year record of Indian summer monsoon dynamics recorded by eastern equatorial Indian Ocean upper water-column structure. *Quat. Sci. Rev.* **77,** 167-180 (2013).

42. Budziak, D. *et al*. Late Quaternary insolation forcing on total organic carbon and C_{37} alkenone variations in the Arabian Sea. *Paleoceanography*. **15,** 307-321 (2000).

43. Ziegler, M. *et al*. Precession phasing offset between Indian summer monsoon and Arabian Sea productivity linked to changes in Atlantic overturning circulation. *Paleoceanography*. **25,** PA3213 (2010).

44. Reichart, G. –J., Lourens, L. J. & Zachariasse, W. J. Temporal variability in the northern Arabian Sea Oxygen Minimum Zone (OMZ) during the last 225,000 years. *Paleoceanography*. **13,** 607-621 (1998).

45. Meissner, T. & Wentz, F. J. Remote Sensing Systems SMAP Ocean Surface Salinities [Level 3 Monthly], Version 2.0 validated release. Remote Sensing Systems, Santa Rosa, Ca, USA. 2016. Available online at www.remss.com/missions/smap.

46. Boyer, T. P. *et al. World Ocean Database 2013.* (NEDSIS, Silver Spring, 2013).

47. Barker, S. *et al*. Icebergs not the trigger for North Atlantic cold events. *Nature*. **520,** 333-336 (2015).

48. Kudrass, H. R., Hofmann, A., Doose. H., Emeis, K. & Erlenkeuser. H. Modulation and amplification of climatic changes in the Northern Hemisphere by the Indian summer monsoon during the past 80 k.y. *Geology*. **29,** 63-66 (2001).

49. Rashid, H., Flower, B. P., Poore, R. Z. & Quinn, T. M. A ~25 ka Indian Ocean monsoon variability record from the Andaman Sea. *Quat. Sci. Rev.* **26,** 2586-2597 (2007).

50. Saraswat, R., Lea, D. W., Nigam, R., Mackensen, A. & Naik. D. K. Deglaciation in the tropical Indian Ocean driven by interplay between the regional monsoon and global teleconnections. *Earth Planet. Sci. Lett.* **375,** 166-175 (2013).

51. Pahnke, K. & Sachs, J. P. Sea surface temperatures of southern midlatitudes 0-160 kyr B. P. *Paleoceanography.* **21,** PA2003 (2006).
52. Jouzel, J. *et al.* Orbital and Millennial Antarctic Climate Variability over the Past 800,000 Years. *Science*. **317,** 793-795 (2007).
53. Deaney, E. L., Barker, S. & van de Flierdt. T. Timing and nature of AMOC recovery across Termination 2 and magnitude of deglacial CO_2 change. *Nat. Commun.* **8,** 14595 (2017).

Acknowledgements

We thank Peter Webb for his help with setting up pXRF analysis, Hilary Sloane for her help with stable isotope analysis, P. Divakar Naidu for providing 2005 NBBT sediment traps. We thank three anonymous reviewers for their insightful comments and suggestions that improved this manuscript. P. A. and K.N-K. acknowledge funding through a NERC PhD grant (NE/L002493/1) associated with the CENTA Doctoral Training Partnership. Samples were provided by the International Ocean Discovery Program (IODP). Stable isotope analysis of planktic foraminifera was funded by NIGFSC grant IP-1649-1116 to P.A.

Author contributions

P.A. conceived the research idea and further developed it with K.N-K. K.N-K processed samples, picked foraminifera, and conducted foraminifera cleaning and trace element analysis under guidance from P.A. and S.M. M.J.L. over saw the stable isotope analysis and S.J.H. helped with trace element analysis. S.C.C. produced benthic oxygen isotope data for age model development. K.N-K., P.A. and P.F.S. discussed the data interpretation and wrote the manuscript, and all authors contributed to the final text.

Competing interests

The authors declare no competing interests.

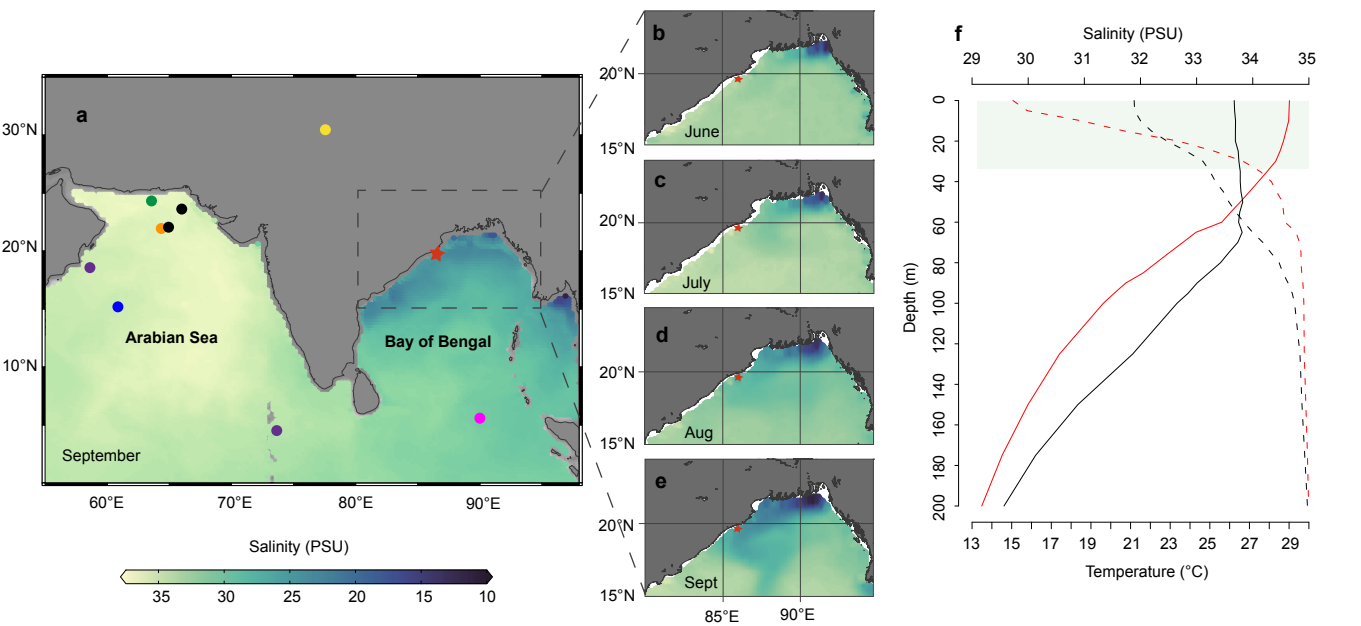
a
30°N
20°N
10°N
60°E
70°E
80°E
90°E
Arabian Sea
Bay of Bengal
September
Salinity (PSU)
35
30
25
20
15
10
b
June
c
July
d
Aug
e
Sept
20°N
15°N
85°E
90°E
f
Salinity (PSU)
29
30
31
32
33
34
35
Depth (m)
0
20
40
60
80
100
120
140
160
180
200
13
15
17
19
21
23
25
27
29
Temperature (°C)

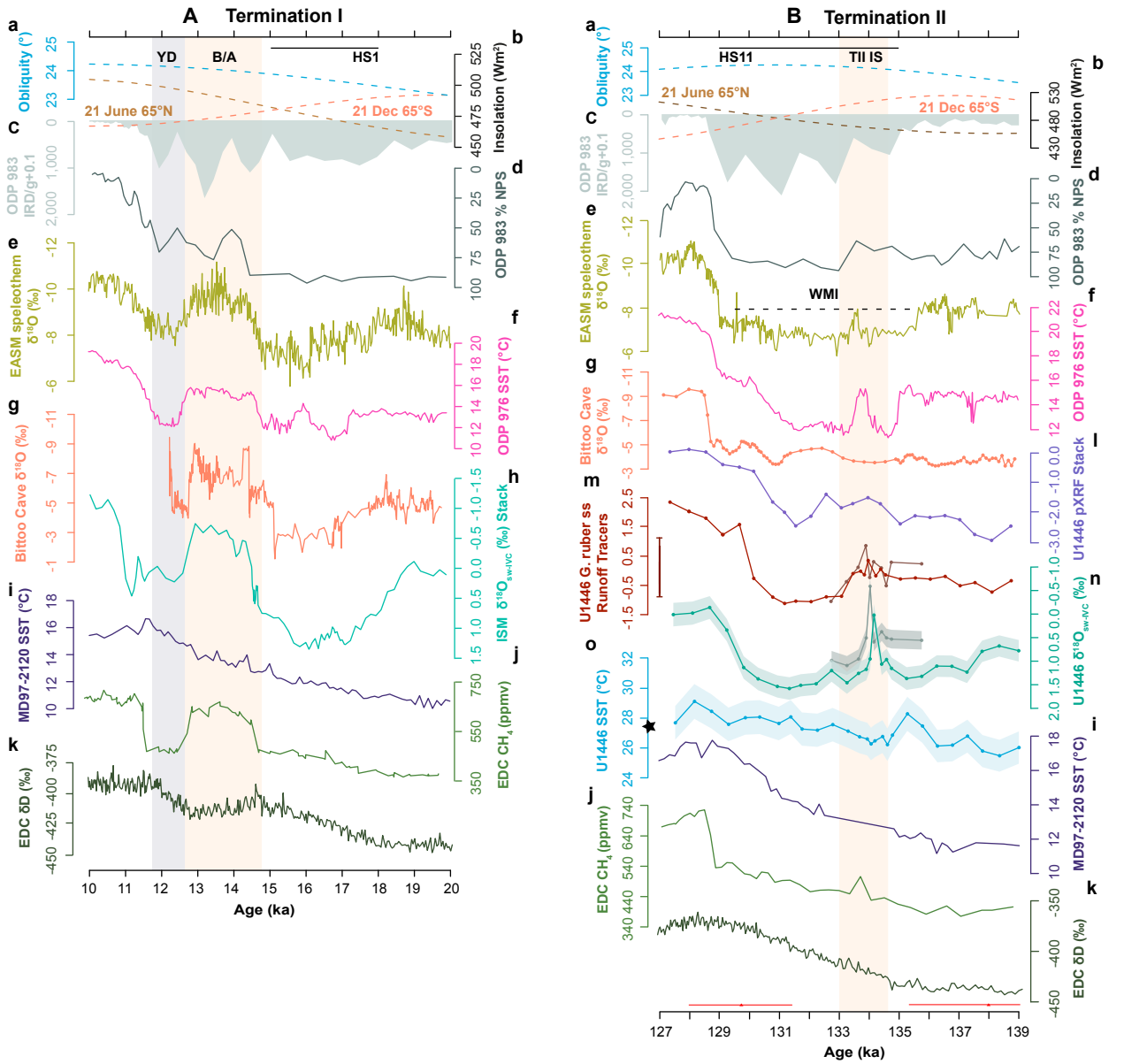
A Termination I
B Termination II
YD
B/A
HS1
HS11
TII IS
21 June 65°N
21 Dec 65°S
Obliquity (°)
Insolation (Wm²)
ODP 983 IRD/g+0.1
ODP 983 % NPS
EASM speleothem δ18O (‰)
WMI
ODP 976 SST (°C)
Bittoo Cave δ18O (‰)
ISM δ18Osw-VC (‰) Stack
U1446 pXRF Stack
U1446 G. ruber ss Runoff Tracers
U1446 δ18Osw-VC (‰)
U1446 SST (°C)
MD97-2120 SST (°C)
EDC CH4 (ppmv)
EDC δD (‰)
Age (ka)

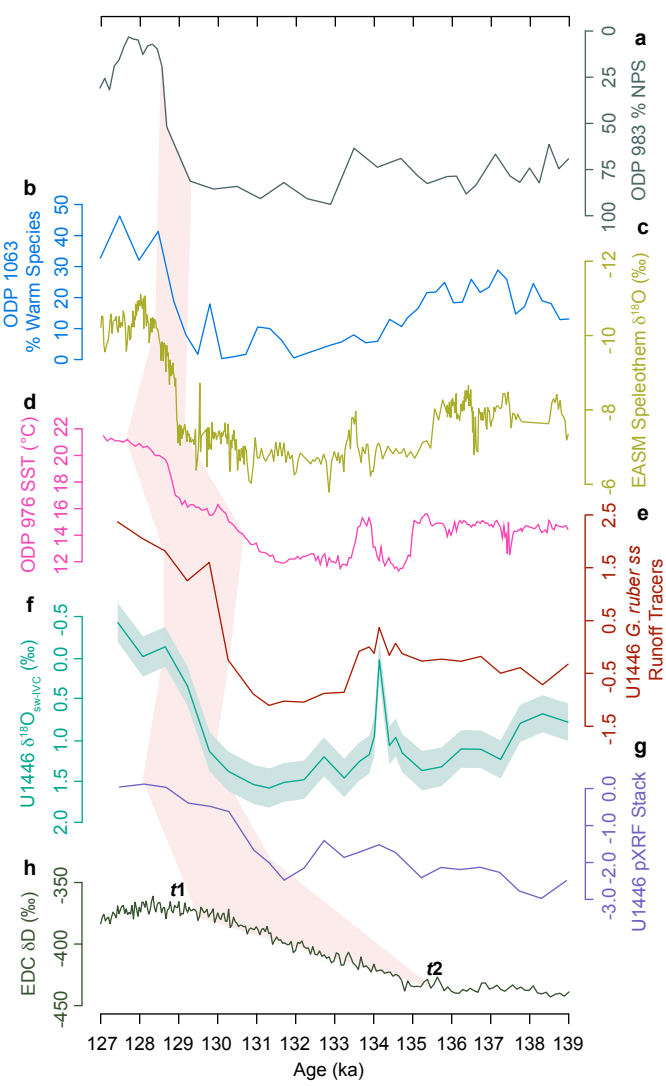
a
ODP 983 % NPS
0 25 50 75 100
b
ODP 1063
% Warm Species
0 10 20 30 40 50
c
EASM Speleothem δ18O (‰)
-12 -10 -8 -6
d
ODP 976 SST (°C)
12 14 16 18 20 22
e
U1446 G. ruber ss
Runoff Tracers
2.5 1.5 0.5 -0.5 -1.5
f
U1446 δ18Osw-IVC (‰)
-0.5 0.0 0.5 1.0 1.5 2.0
g
U1446 pXRF Stack
0.0 -1.0 -2.0 -3.0
h
EDC δD (‰)
-350 -400 -450
t1
t2
127 128 129 130 131 132 133 134 135 136 137 138 139
Age (ka)

Correspondence should be addressed to katrina.kerr@open.ac.uk and **requests for materials** to pallavi.anand@open.ac.uk

Figure 1. ISM induced freshening in the Bay of Bengal a) Map depicting ISM inferred wind-driven upwelling and stratification records (as circles: pink[41], purple[42], blue[9], orange[44], black[45] and green[10]) that extend across TII. Yellow circle indicates Bittoo cave[2]. b-e) Average monthly sea surface salinity during 2017 ISM months[45] exhibiting proliferation of fluvial input. Site U1446 is indicated by red star. f) Winter (black) and summer (red) monsoon season temperature (solid) and salinity (dashed) depth profiles[46] above Site U1446. Shaded bar indicates inferred depth range of *G. ruber ss*. Figure created using Ocean Data View software (http://odv.awi.de/).

Figure 2. Sequence of global events across TI (A) and TII (B) a) Obliquity[33] b) June 21st and December 21st insolation[33] c) ODP 983, North Atlantic, IRD[47] d) ODP 983 % NPS[47] e) EASM speleothem $\delta^{18}O$[6] f) ODP 976, western Mediterranean, SST[26, 28] g) Bittoo Cave speleothem $\delta^{18}O$[2] h) ISM $\delta^{18}O_{sw\text{-}IVC}$ stack[48-50] i) MD97-2120, southwest Pacific, SST[51] j) EDC CH_4[37, 12] k) EDC δD[52, 12] l) U1446 pXRF stack m) U1446 *G. ruber ss* (red) and *N. dutertrei* (brown) runoff tracers. Red bar shows modern sediment trap data range n) U1446 *G. ruber ss* (green) and *N. dutertrei* (grey) $\delta^{18}O_{sw\text{-}IVC}$ and o) U1446 SST. Star represents modern day mean annual SST at study site[46]. Shaded envelopes represent 1σ (Methods). Red triangles represent age control points contained within interval shown and associated AICC2012 chronology errors[12] (Methods).

Figure 3. TII onset and duration a) ODP 983, North Atlantic, % NPS[47] on AICC2012 chronology[12] b) ODP 1063, Atlantic Ocean, % Warm species[53] on AICC2012 chronology[12] c) EASM speleothem $\delta^{18}O$[6] d) ODP 976, western Mediterranean Sea, SST[28] on Corchia Cave radiometrically constrained chronology[26] e) U1446 *G. ruber ss* runoff tracers (this study) f) U1446 *G. ruber ss* $\delta^{18}O_{sw\text{-}IVC}$ (this study) g) U1446 pXRF stack h) EDC δD[52] on AICC2012 chronology[12]. Pink shaded area denotes *t*2 (deglaciation onset) and *t*1 (attainment of interglacial) as modelled using RAMPFIT[35] (Methods).

Methods

Site U1446 (19º5.02'N, 85º44'E) was drilled during IODP Expedition 353 and located at a depth of 1430 meters below sea level in the Mahanadi Basin[54]. The BoB represents the core convective region of the ISM due to the thermodynamic structure of the water column resulting in positive ocean-atmosphere feedbacks favouring high SSTs (>28ºC) allowing convection to be sustained during the summer monsoon months of June through to September[55]. The ISM exerts a strong seasonal signature of surface water freshening and stratification within the BoB due to a net surface water exchange of 184 x 10^{10} m^3 during the ISM months[56]. ISM induced river runoff generates a north-south salinity gradient; the northern BoB undergoes a reduction in salinity of 9% during this period[57].

Age Model

The much expanded nature of the sediment sequence at Site U1446 (~25 cm/ka), and consequent high fidelity of our palaeoclimatic records, significantly reduces the error of the duration of events and the rates of change inferred from our records[58]. Using Analyseries[59] we graphically correlated benthic foraminifera (*Uvigerina spp.* and *Cibicidoides wuellerstorfi*) $\delta^{18}O$ (Clemens, S. C., unpublished data) to benthic $\delta^{18}O$ from south Pacific core PS75/059-2[60] (Supplementary Fig. 1a). This itself is tied to the AICC2012 chronology[12] by exploiting the

age-depth relationship from PS75/059-2 Fe dust flux record[61] which has been tuned to the EDC Antarctic ice core[61, 62] (Supplementary Fig. 2). Tuning to AICC2012 was chosen rather than the absolute dated EASM speleothem record to allow for independent assessment of the lead/lag relationship between the ISM and the EASM. We infer that our records are not biased to the high latitudes of the southern hemisphere by our tuning strategy due to synchronicity existing between the Chinese Loess magnetic susceptibility record with EDC Antarctic ice core dust fluxes[62]. To ascertain our confidence in our age model, we further tied U1446 benthic $\delta^{18}O$ to ODP Leg. 117, Site 1146 benthic $\delta^{18}O$ which has been transferred to the speleothem chronology[63]. We present site U1446 benthic $\delta^{18}O$ on three different age models (AICC2012[12], RC2011[63] and LR04[64]) (Supplementary Fig. 1c) in order to confirm the lead of U1446 ISM records over the EASM across TII regardless of chronology (Supplementary Fig. 3).

We used Bchron[65], a Bayesian probability model, to model the 95% uncertainty envelope between tie points with the AICC2012 chronology error (modelled as Gaussian distribution) of EPICA Dome C at those points[12] (Supplementary Fig. 1b).

All datasets used to assess relative lead and lag relationships are on a consistent age-model; that of AICC2012[12] or absolute radiometrically constrained chronology[2, 6, 26] (see original references for detail).

Foraminiferal stable isotope and trace metal analysis

The planktic foraminifera *Globigerinoides ruber sensu-stricto (ss)*, was identified using the taxonomic description in ref. 66. Between 6 to 30 individuals were picked from the 250-355μm size-fraction and gently crushed prior to analysis. Oxygen isotope analyses were performed at the British Geological Survey, NERC Isotope Geoscience Facilities, Keyworth using an Isoprime dual inlet mass spectrometer with Multiprep device. The reproducibility of oxygen isotope measurements is ±0.05‰ (1σ) based on replicate measurements of carbonate standards. All data are reported in the usual delta notation ($\delta^{18}O$) in ‰ on the VPDB scale.

For trace metal analysis, samples were cleaned using a modification of the method described in ref. 19 and reversal of the oxidative and reductive steps[67]. Due to the proximal setting of Site U1446 an extended clay removal step was essential in order to ensure removal of any fine clays that may bias Mg content in carbonate samples. Samples were initially rinsed with repeated MQ and methanol rinses with ultrasonification of 40 seconds between each rinse. Samples were then inspected under a microscope and any discoloured fragments, fragments with pyrite or silicate particles were removed. Subsequently samples were subjected to a reductive and 10% oxidative step to ensure removal of any coatings and organics. Samples were then polished using a weak (0.001M) HNO_3 leaching step and dissolved (0.075M HNO_3) on the day of analysis. Samples were analysed at the Open University using an Agilent Technologies Triple-Quad ICP-MS. Contaminant ratios (Al/Ca and Fe/Ca) were monitored in order to assess any clay and organic contaminations (Supplementary Fig. 4).

Estimating temperature and $\delta^{18}O_{sw}$

The addition of a reductive step during foraminiferal trace element cleaning has been shown to reduce Mg/Ca values[68]. Following ref. 69, we apply a correction for a 10% reduction in Mg/Ca associated with the reductive method due to the chosen temperature calibration being based on analysis using only the oxidative step[70]. The Mg/Ca temperature calibration used was accordingly adjusted:

$$Mg/Ca = 0.38(\pm0.02) \exp((0.09\pm0.003)*T)^{70}$$

$$\text{Adjusted } Mg/Ca = 0.342\exp(0.09T)$$

An ice volume correction was applied to the calcite $\delta^{18}O_c$ following the Red Sea Level Curve (95% probability maximum)[71] with a conversion factor $\delta^{18}O$ enrichment of 0.008‰ per meter sea level lowering applied[72]:

$$\delta^{18}O_{IVC}(t) = \delta^{18}O(t) + (RSL(t) * 0.008)$$

The temperature estimates derived from Mg/Ca and the measured calcite $\delta^{18}O_c$ of planktic foraminifera allows for the derivation of seawater $\delta^{18}O_{sw}$:

$$T°C = 14.9(\pm0.1) - 4.8(\pm0.08)*(\delta^{18}O_c - \delta^{18}O_{sw}) - 0.27‰^{73}$$

The $\delta^{18}O_{sw}$ has been shown to correlate strongly with salinity in the northern BoB. Factors controlling this relationship include precipitation, river runoff and evaporation thus during the summer monsoon months precipitation and runoff exceeds evaporation promoting a low $\delta^{18}O_{sw}$-Salinity Slope[74, 75]. However, we do not convert U1446 $\delta^{18}O_{sw}$ to salinity using modern day calculated regressions due to observation of significant spatiotemporal variations and uncertainties in assumptions associated with extending these relationships into the past[74]. Furthermore, recent work has indicated the potential control salinity exerts on Mg-incorporation in foraminiferal calcite[76]. Low salinity during the warmer ISM season may potentially dampen our reconstructed SSTs based on Mg/Ca relative to actual SST however, there would be a limited overall effect on the reconstructed $\delta^{18}O_{sw}$.

N. dutertrei is typically inferred to represent thermocline conditions (~70-120m) accompanying the deep chlorophyll maximum[77, 78]. However, across the TII IS *N. dutertrei* shows more depleted $\delta^{18}O_{sw\text{-}IVC}$ values than surface dwelling *G. ruber ss* (Fig. 2B n). We infer that this is associated with the unique hydrographic conditions that Site U1446 experiences and that *N. dutertrei* occupies a shallower depth, in the freshwater lens of the upper water column, than what is typically inferred. Additionally, available Mg/Ca calibrations based on upper thermocline habitat, and therefore a narrower temperature range, underestimates the temperature values for *N. dutertrei* thus resulting in more depleted $\delta^{18}O_{sw\text{-}IVC}$ values as the calcite $\delta^{18}O$ values are more enriched than *G. ruber ss* (Supplementary Fig. 5). During the TII IS, *G. ruber ss* and *N. dutertrei* $\delta^{18}O_{sw\text{-}IVC}$ is decoupled by ~100 years (Fig. 2B n) highlighting the vertical flux of ISM induced freshening.

462 Error propagation of the temperature and $\delta^{18}O_{sw}$ estimates was calculated using the following
463 equations[79] where Mg/Ca standard deviation is 0.029mmol/mol^{-1} and $\delta^{18}O_c$ is 0.05‰ based on
464 repeated analysis of internal standards. The error propagation is based on assumptions of no
465 covariance among a, b, T and $\delta^{18}O_c$[79]:

466 $$\sigma_T^2 = \left(\frac{\partial T}{\partial a}\sigma_a\right)^2 + \left(\frac{\partial T}{\partial b}\sigma_b\right)^2 + \left(\frac{\partial T}{\partial Mg/Ca}\sigma_{Mg/Ca}\right)^2$$

467 where:

468 $$a = 0.342(\pm 0.02)\ ^{70}$$

469 $$b = (0.09\pm 0.003)\ ^{70}$$

470 $$\frac{\partial T}{\partial a} = -\frac{1}{a^2}\ln\left(\frac{Mg/Ca}{b}\right)$$

471 $$\frac{\partial T}{\partial b} = -\frac{1}{ab}$$

472 $$\frac{\partial T}{\partial Mg/Ca} = \frac{1}{a} \times \frac{1}{Mg/Ca}$$

473 $$\sigma_{\delta^{18}O_{sw}}^2 = \left(\frac{\partial \delta^{18}O_{sw}}{\partial T}\sigma_T\right)^2 + \left(\frac{\partial \delta^{18}O_{sw}}{\partial a}\sigma_a\right)^2 + \left(\frac{\partial \delta^{18}O_{sw}}{\partial b}\sigma_b\right)^2 + \left(\frac{\partial \delta^{18}O_{sw}}{\partial \delta^{18}O_c}\sigma_{\delta^{18}O_c}\right)^2$$

474 where:

475 $$a = 14.9(\pm 0.1)\ ^{73}$$

476 $$b = -4.8(\pm 0.08)\ ^{73}$$

477 $$\frac{\partial \delta^{18}O_{sw}}{\partial T} = -\frac{1}{b}$$

478 $$\frac{\partial \delta^{18}O_{sw}}{\partial a} = \frac{1}{b}$$

$$\frac{\partial \delta^{18}O_{sw}}{\partial b} = \frac{T}{b^2} - \frac{a}{b^2}$$

$$\frac{\partial \delta^{18}O_{sw}}{\partial \delta^{18}O_c} = 1$$

To further constrain errors associated with calculating SST and $\delta^{18}O_{sw}$ we used Paleo-Seawater Uncertainty Solver (PSUSolver)[80]. PSUSolver models uncertainties associated with age model, calibrations, analytical and sea level estimate errors by performing bootstrap Monte Carlo simulations[80]. Accounting for AICC2012 age model errors[12] we input an average age model error of 2 ka and analytical errors; Mg/Ca of 0.029mmol/mol^{-1} and $\delta^{18}O_c$ is 0.05‰, in order for PSUSolver to probabilistically constrain the median estimate and confidence intervals for SST and $\delta^{18}O_{sw}$ (Supplementary Fig. 6a). To assess the influence age model error exerts on U1446 SST and $\delta^{18}O_{sw}$ we also input an age model error of 1 ka (Supplementary Fig. 6b) and 0 ka (Supplementary Fig. 6c). This indicates that age model errors exert the strongest influence on PSUSolver SST and $\delta^{18}O_{sw}$. An average age model error of 2 ka renders the TII IS inconspicuous. However, we have confidence in our original U1446 SST and $\delta^{18}O_{sw}$ interpretations despite the associated errors with the AICC2012 chronology owing to TII IS having been resolved in other independently dated records (Fig. 2B) and the coherence of U1446 $\delta^{18}O_{sw}$ with deglacial warming in western Mediterranean Sea SST records from ODP Site 976[28] (Fig. 3) that has a radiometrically constrained age model[26].

Interpreting Mn/Ca, Nd/Ca & U/Ca as river runoff proxies

Mn/Ca ratios measured in foraminifera are typically used as an indicator of contamination of foraminifer calcite from authigenic Mn-rich oxide coatings on the foraminifer shell. Our Mn/Ca data display no correlation with Mg/Ca (r^2=0.0894), strongly arguing against the presence of Mn-rich oxide coatings on our foraminifera that would bias our Mg/Ca-derived SSTs. The foraminifera cleaning method applied in this study had the reductive cleaning step included,

502 which ensures removal of Fe-Mn coatings, added on the carbonate tests at the sediment-water
503 interface[19, 68]. Mn/Ca correlates with Nd/Ca and U/Ca (Supplementary Fig. 7), reinforcing
504 evidence that these elements are delivered to our study site via fluvial runoff and can thus be
505 used as runoff proxies in this proximal setting. High fluvial fluxes in the BoB reflect the
506 monsoon region's vigorous hydrological and concomitant weathering regime. This is
507 expressed by the vast quantities of material discharged via the rivers; the Ganges-Brahmaputra
508 systems contribute alone 1.06×10^9 tonnes of sediment annually[81]. Such a unique hydrographic
509 setting allows high concentrations of dissolved lithogenic elements (Mn, Nd, U) to be
510 precipitated (either as authigenic or biogenic carbonate phases) upon mixing with seawater.
511 The observed concentrations of these elements at Site U1446 are well beyond the
512 concentrations that are typically found in planktic foraminifera[20]. Similarly, elevated levels of
513 Mn/Ca, Nd/Ca and U/Ca ratios have been found in planktic foraminifera from Ceara Rise, ODP
514 Site 926, receiving amazon fluvial fluxes[82, 83]. Furthermore, we generated trace element data
515 for *G. ruber ss* from NBBT-05-S sediment trap from the northern BoB. The range of values
516 exhibited by this runoff tracers record (Mn, Nd and U) overlaps with the range found in the
517 NBBT-05-S sediment trap data (Fig. 2B m). Thus, we interpret Mn/Ca, Nd/Ca and U/Ca ratios
518 in *G. ruber ss* (Supplementary Fig. 8) as a proxy for fluvial runoff at marginal sites and suggest
519 that they could be further ground-truthed for application in other marginal marine settings.
520 Owing to the similarity between Mn/Ca, Nd/Ca and U/Ca we normalise using the standard
521 deviation[21]:

522 $$/\mathrm{Ca(t)}_{\mathrm{norm}} = \frac{/\mathrm{Ca(t)} - \overline{/\mathrm{Ca}}}{\sigma(/\mathrm{Ca})}$$

523 Where:

524 /Ca(t) (e.g. Mn/Ca) represents the trace element to Ca ratio at a given time.

525 $\overline{/Ca}$ represents the mean of all the trace element to Ca ratios (e.g. Mn/Ca) across study
526 interval.

527 $\sigma(/Ca)$ represents the standard deviation of the trace element to Ca ratio across study interval.

528 Subsequently we average these values ($/Ca(t)_{norm}$) for each of the tracers to produce a factor
529 representing *G. ruber ss* runoff tracers. Furthermore, there is a similar signature among these
530 tracers with the data gained from pXRF (Supplementary Fig. 9).

531 **Discrete portable X-Ray Fluorescence Analysis**

532 Analysis of major and minor elements was performed using a Niton XL3t900 portable X-Ray
533 Fluorescence (pXRF). Prior to analysis 5 grams of material was weighed, dried in an oven at
534 40ºC and subsequently homogenized into a fine powder through use of a pestle and mortar.
535 The powdered material was transferred into 7ml vials, sealed tightly with non-PVC Clingfilm
536 and placed flush over the aperture of the X-ray emitter (Saker-Clark, M., per comms).
537 Calibration for each element of interest was performed through analysis of geochemical in-
538 house and reference powdered rock standards with known concentrations. A set of internal and
539 reference standards were run every 10th sample for quality control (Supplementary Table 1).
540 Bulk sediment elemental geochemistry is controlled by detrital (i.e. terrigenous input via river
541 runoff) and authigenic processes. Therefore, in order to reconstruct ISM derived river runoff a
542 selection of inferred terrigenous derived elements were selected to represent increased fluvial
543 runoff and detrital input to the site; Ti, K, Al and Rb (Supplementary Fig. 9). These elements
544 were combined through normalising to unit variance (described in the above section for *G.*
545 *ruber ss* runoff tracers) to produce a factor of pXRF runoff element variations[21] due to showing
546 strong correlation with each other (Supplementary Fig. 10). In order to clarify the inconsistency
547 in elements chosen to represent fluvial runoff between the pXRF element stack and the *G.*
548 *ruber ss* tracers: i) Uranium concentrations in discrete U1446 samples were below detection

limit and Nd was not measured and ii) Mn concentrations in ocean sediments is complicated by redox processes and therefore, not a suitable candidate for representing the detrital phase in bulk sediment elemental profiles. We infer that due to increased terrigenous supply during a strengthened ISM, reduced bottom water conditions are established, resulting in Mn reduction and dissolution into pore waters due to the increased solubility of reduced Mn (Mn^{2+})[84-87]. In contrast, during times of weaker ISM and reduced terrigenous supply, aerobic conditions promote formation of solid-phase Mn oxyhdroxides and thus increase in Mn concentrations in the bulk sediment (Supplementary Fig. 9)[84-87]. This reasoning is coherent with conditions found in the Cariaco Basin, proximal to high terrigenous fluxes via river runoff[88].

Detection of TII Change Points

In order to empirically assess deglaciation onset during TII we employed the RAMPFIT[35] algorithm. RAMPFIT segments the data into three parts using a weighted least squares regression and brute force to find two breakpoints denoted as *t*1 and *t*2[35]. RAMPFIT was used to estimate deglaciation onset (*t*1) and duration (*t*2) in the EASM speleothem $\delta^{18}O$ record[6], ODP 976 western Mediterranean Sea SST[26,28], ODP 1063 % warm species[53], ODP 983 % NPS[47], EPICA Dome C δD[52] and U1446 $\delta^{18}O_{sw}$, *G. ruber ss* runoff tracers and pXRF stack (Fig. 3). These records were chosen in order to identify the proliferation of deglaciation across the NH having propagated from the SH. 400 iterations of wild bootstrap with seed generator number of 400 was used to determine the uncertainties (Supplementary Table. 2).

Comparison of TII with TI

The same methods described above were employed to characterise deglaciation across TI (Supplementary Fig. 10). Our results for TII demonstrate the sequence of deglaciation having been driven from the SH, a lagged NH response and the ISM contributing to the inter-hemispheric transfer of heat and moisture. Furthermore, we highlight the out-of-phase behaviour between the EASM and ISM (Fig. 3). However, this is in contrast to the sequence

of events across TI in which the ISM appears to be in-phase with the EASM and other NH climate records (Supplementary Fig. 11). Our results from TII thus exemplify the heterogeneity between TI and TII that draws on previous work in which orbital preconditioning is regarded as the driver in dictating the internal climate feedback response[89, 90]. Furthermore, the behaviour of the ISM during TII may be a result of the anomalous orbital conditions which stray from classic Milankovitch theory[91]. The early rise in NH solar insolation during TI is thought to have initiated deglaciation with rapid NH ice sheet retreat occurring from ~19-20 ka[92] resulting in AMOC shutdown and subsequent warming in the SH[93]. This is in contrast to TII where the earlier rise in SH summer insolation occurs 10 ka prior to NH solar insolation increase[25, 94]. We postulate based on the opposing hemispheric controls on the ISM during TI and TII that the ISM is not hemispherically biased but is governed by inter-hemispheric climate controls in comparison to the predominantly NH-forced EASM[6].

Methods References

54. Clemens, S. C. *et al*. Indian Monsoon Rainfall. *Proceedings of the International Ocean Discovery Program.* **353,** (2016).
55. Shenoi, S. S. C., Shankar, D. & Shetye, S. R. Differences in heat budgets of the near-surface Arabian Sea and Bay of Bengal: implications for the summer monsoon. *J. Geophys. Res. Oceans.* **107,** 2052 (2002).
56. Varkey, M. J., Murty, V. S. N. & Suryanarayana, A. Physical oceanography of the Bay of Bengal and Andaman Sea. *Oceanogr. Mar. Biol. Annu. Rev.* **34,** 1-70 (1996).
57. Levitus, S. & Mishonov, A. *World Ocean Atlas 2013, Volume 2: Salinity* (NESDIS, Silver Spring, 2013).
58. Kemp, D. B. & Sexton, P. F. Time-scale uncertainty of abrupt events in the geologic record arising from unsteady sedimentation. *Geology.* **42,** 891-894 (2014).

59. Paillaird, D., Labeyrie, L. & Yiou, P. Macintosh Program performs time-series analysis. *EOS.* **77,** 379 (1996).

60. Ullermann, J. *et al*. Pacific-Atlantic Circumpolar Deep Water coupling during the last 500 ka. *Paleoceanography.* **31,** 639-650 (2016).

61. Lamy, F. *et al*. Increased Dust Deposition in the Pacific Southern Ocean During Glacial Periods. *Science.* **343,** 403-407 (2014).

62. Lambert, F. *et al*. Dust-climate couplings over the past 800,000 years from the EPICA Dome C ice core. *Nature.* **452,** 616-619 (2008).

63. Caballero-Gill, R. P., Clemens, S. C. & Prell, W. L. Direct correlation of Chinese speleothem $\delta^{18}O$ and South China Sea planktonic $\delta^{18}O$: Transferring a speleothem chronology to the benthic marine chronology. *Paleoceanography.* **27,** PA2203 (2012).

64. Lisiecki, L. E. & Raymo, M. E. A Pliocene-Pleistocene stack of 57 globally distributed $\delta^{18}O$ records. *Paleoceanography*. **20,** PA1003 (2005).

65. Haslett, J. & Parnell, A. A simple monotone process with application to radiocarbon-dated depth chronologies. *Stat Soc Ser C Appl Stat.* **57,** 339-418 (2008).

66. Wang, L. Isotopic signals in two morphotypes of *Globigerinoides ruber* (white) from the South China Sea: implications for monsoon climate change during the last glacial cycle. *Palaeogeogr. Palaeoclimatol. Palaeoecol.* **161,** 381-394 (2000).

67. Rosenthal, Y., Boyle, E. A. & Labeyrie, L. Last glacial maximum paleochemistry and deepwater circulation in the Southern Ocean: Evidence from foraminiferal cadmium. *Paleoceanography.* **12,** 787-796 (1997).

68. Barker, S., Greaves, M. & Elderfield. H. A study of cleaning procedures used for foraminiferal Mg/Ca paleothermometry. *Geochem. Geophys. Geosyst.* **4,** 8407 (2003).

69. Gibbons, F. T. *et al*. Deglacial $\delta^{18}O$ and hydrologic variability in the tropical Pacific and Indian Oceans. *Earth Planet Sci. Lett.* **387,** 240-251 (2014).

70. Anand, P., Elderfield, H. & Conte, M. H. Calibration of Mg/Ca thermometry in planktonic foraminifera from a sediment trap time series. *Paleoceanography*. **18,** 1050 (2003).

71. Grant, K. M. *et al*. Rapid coupling between ice volume and polar temperature over the past 150,000 years. *Nature.* **491,** 744-747 (2012).

72. Adkins, J. F., McIntyre, K. & Schrag, D. P. The Salinity, Temperature, and $\delta^{18}O$ of the Glacial Deep Ocean. *Science.* **298,** 1769-1773 (2002).

73. Bemis, B. E., Spero, H. J., Bijma. J. & Lea, D. W. Reevaluation of the oxygen isotopic composition of planktonic foraminifera: Experimental results and revised paleotemperature equations. *Paleoceanography*. **13,** 150-160 (1998).

74. Singh, A., Jani, R. A. & Ramesh, R. Spatiotemporal variations of the $\delta^{18}O$-salinity relation in the northern Indian Ocean. *Deep-Sea. Res. I.* **57,** 1422-1431 (2010).

75. Delaygue, G. *et al.* Oxygen isotope/salinity relationship in the northern Indian Ocean. *J. Geophys. Res.* **106,** 4565-4574 (2001).

76. Gray, W. R. *et al*. The effects of temperature, salinity, and the carbonate system on Mg/Ca in *Globigerinoides ruber* (white): A global sediment trap calibration. *Earth. Planet. Sci. Lett.* **482,** 607-620 (2018).

77. Ravelo, A. C. & Fairbanks, R. G. Oxygen Isotopic Composition of Multiple Species of Planktonic Foraminifera: Recorders of the Modern Photic Zone Temperature Gradient. *Paleoceanography.* **7,** 815-831 (1992).

78. Mohtadi, M. *et al*. Reconstructing the thermal structure of the upper ocean: Insights from planktic foraminifera shell chemistry and alkenones in modern sediments of the tropical eastern Indian Ocean. *Paleoceanography.* **26,** PA3219 (2011).

79. Bevington, P. R. & Robinson, K. D. *Data Reduction and Error Analysis for the Physical Sciences 3rd edn* (McGraw-Hill, 2003).

80. Thirumalai, K., Quinn, T. M. & Marino, G. Constraining past seawater $\delta^{18}O_{sw}$ and temperature records developed from foraminiferal geochemistry. *Paleoceanography.* **31,** 1409-1422 (2016).
81. Milliman, J. D. & Syvitski, J. P. M. Geomorphic/Tectonic Control of Sediment Discharge to the Ocean: The Importance of Small Mountainous Rivers. *J. Geol.* **100,** 525-544 (1992).
82. Stewart, J. A., James, R. H., Anand. P. & Wilson, P. A. Silicate Weathering and Carbon Cycle Controls on the Oligocene-Miocene Glaciation. *Paleoceanography.* **32,** 1070-1085 (2017).
83. Stewart, J. A., Gutjahr, M., James, R. H., Anand, P. & Wilson, P. A. Influence of the Amazon River on the Nd isotope composition of deep water in the western equatorial Atlantic during the Oligocene-Miocene transition. *Earth. Planet. Sci. Lett.* **454,** 132-141 (2016).
84. Calvert, S. E. & Price, N. B. Diffusion and reaction profiles of dissolved manganese in the pore waters of marine sediments. *Earth Planet. Sci. Lett.* **16,** 245-249 (1972).
85. Thomson, J., Higgs, N. C., Croudace, I. W., Colley, S. & Hydes, D. J. Redox zonation of elements at an oxic/post-oxic boundary in deep-sea sediments. *Geochim. Cosmochim. Acta.* **57,** 579-595 (1993).
86. Calvert, S. E. & Pedersen, T. F. Geochemistry of Recent oxic and anoxic marine sediments: Implications for the geological record. *Mar Geol.* **113,** 67-88 (1993).
87. Burdige, D. J. The biogeochemistry of manganese and iron reduction in marine sediments. *Earth. Sci. Rev.* **35,** 249-284 (1993).
88. Yarincik, K. M., Murray, R. W., Lyons, T. W., Peterson, L. C. & Haug, G. H. Oxygenation history of bottom waters in the Cariaco Basin, Venezuela, over the past

578,000 years: Results from redox-sensitive metals (Mo, V, Mn, and Fe). *Paleoceanography*. **15,** 593-604 (2000).

89. Carlson, A. E. Why there was not a Younger Dryas-like event during the Penultimate Deglaciation. *Quat. Sci. Rev.* **27,** 882-887 (2008).

90. Alley, R. B., Brook, E. J. & Anandakrishnan, S. A northern lead in the orbital band: north-south phasing of Ice-Age events. *Quat. Sci. Rev.* **21,** 431-441 (2002).

91. Hays, J. D., Imbrie, K. & Shackleton, N. J. Variations in the Earth's Orbit: Pacemaker of the Ice Ages. *Science*. **194,** 1121-1132 (1974).

92. Clark, P. U. *et al*. The Last Glacial Maximum. *Science.* **325,** 710-714 (2009).

93. He, F. *et al*. Northern Hemisphere forcing of Southern Hemisphere climate during the last deglaciation. *Nature*. **494,** 81-85 (2013).

94. Masson-Delmotte, V. *et al.* Abrupt change of Antarctic moisture origin at the end of Termination II. *Proc. Nat. Acad. Sci.* **107,** 12091-12094 (2010).

Data Availability

Data generated from this study (IODP Exp. 353, Site U1446) are available via the National Geoscience Data Centre (NGDC), DOI: 10.5285/061d77af-a805-4cf0-b969-0b8f042fae74.

Antarctic EDC ice-core records presented on AICC2012 chronology are available from: https://doi.pangaea.de/10.1594/PANGAEA.824883 and https://doi.pangaea.de/10.1594/PANGAEA.824891

The EASM composite speleothem $\delta^{18}O$ record is available from: https://www.ncdc.noaa.gov/paleo-search/study/20450

Bittoo Cave speleothem $\delta^{18}O$ record is available from: https://www.ncdc.noaa.gov/paleo-search/study/20449

ODP 983 and 1063 data is available as a supplementary data set associated with Ref. 53.

ODP 976, western Mediterranean Sea SST data on Corchia radiometrically constrained chronology is available as a supplementary dataset associated with Ref. 26.

Benthic $\delta^{18}O$ of PS75/059-2 is available at: https://doi.org/10.1594/PANGAEA.833422

PS75/059-2 on AICC2012 chronology at: https://doi.org/10.1594/PANGAEA.826580.